

# Lawrence Berkeley National Laboratory

## LBL Publications

### Title

Reflective binary amplitude grating for soft x-ray shearing and Hartmann wavefront sensing.

### Permalink

<https://escholarship.org/uc/item/0zd8r0n8>

### Journal

Optics Letters, 45(17)

### ISSN

0146-9592

### Authors

Goldberg, Kenneth A

Bryant, Diane

Wojdyla, Antoine

et al.

### Publication Date

2020-09-01

### DOI

10.1364/ol.398737

Peer reviewed

# A reflective binary amplitude grating for soft x-ray shearing and Hartmann wavefront sensing

KENNETH A. GOLDBERG<sup>1</sup>, DIANE BRYANT<sup>1</sup>, ANTOINE WOJDYLA<sup>1</sup>, MICHAEL HELMBRECHT<sup>2</sup>, AND ERIC GULLIKSON<sup>3</sup>

<sup>1</sup>Advanced Light Source, Lawrence Berkeley National Laboratory, 1 Cyclotron Road, Berkeley CA, 94720

<sup>2</sup>A.M. Fitzgerald & Associates, 700 Airport Boulevard, Suite 210, Burlingame, CA 94010

<sup>3</sup>Center for X-Ray Optics, Lawrence Berkeley National Laboratory, 1 Cyclotron Road, Berkeley CA, 94720

\*Corresponding author: KAGoldberg@lbl.gov

**We demonstrate a reflective wavefront sensor grating suitable for the characterization of high-quality x-ray beamlines and optical systems with high power densities. Operating at glancing incidence angles, the optical element is deeply etched with a two-level pattern of shearing interferometry gratings and Hartmann wavefront sensor grids. Transverse features block unwanted light, enabling binary amplitude in reflection with high pattern contrast. We present surface characterization and soft x-ray reflectometry of a prototype grating array to demonstrate function prior to wavefront measurement applications. A simulation of device performance is shown.**

A new generation of high-brightness, coherent, short-wavelength synchrotron and free electron laser (FEL) light sources is driving x-ray optical system requirements to preserve the wavefront quality from the source to the sample. Wavefront sensor feedback is essential for the control and optimization of x-ray beamlines with diffraction-limited performance.

Aberrations accrue from every optical element in the beamline. With soft and tender x-ray wavelengths ranging from 0.1 nm to 10 nm, the wavefront quality is measured in fractions of a nanometer. This includes contributions from mirror surface figure errors, misalignment, thermal and mechanical distortions, surface contamination and vibration. For diffractive optical elements, including monochromator gratings and crystals, wavefront quality is affected by line-placement errors as well as substrate quality and distortion. Inhomogeneities in transmission elements can also introduce wavefront phase and amplitude errors.

Feedback for correcting aberrations begins with accurate measurements from wavefront sensors. Among the many techniques that have been reported for soft and tender x-ray applications, shearing interferometry (frequently called *Talbot interferometry*) [1–5] and Hartmann sensing [6, 7] have emerged as the most commonly applied approaches for high accuracy and sensitivity. Their widespread use can be attributed to the fact that they

are straightforward to implement and the measurements can be recorded and analyzed without great effort or computational power. Shearing and Hartmann share similar hardware requirements. Both techniques probe the local wavefront slope, enabling wavefront reconstruction. However, they operate on different principles.

Shearing is an interferometric technique that uses a 1D or 2D grating structure to produce multiple, laterally displaced and overlapping copies of the wavefront at a downstream detection plane. It relies on the beam coherence and on Talbot self-imaging properties to produce high contrast fringes. In shearing, optimal separation distances between the grating and the detection plane are dependent on the wavelength and the grating pitch: maintaining a fixed separation distance across a wide energy range can require the use of several gratings. In principle, the shearing grating can be made from any periodic phase or amplitude structure. Due to differences in material attenuation properties, transmission *phase* structures are commonly used at hard x-ray wavelengths [8], and transmission *amplitude* structures at soft x-ray wavelengths [1, 3].

Hartmann testing is a non-interferometric technique in which a well-characterized grid of holes in an opaque screen projects a 1D or 2D array of spots or lines, with diffraction, onto the detection plane. The grid is designed so the projected spots are distinct and not overlapping. Similar to shearing, when a fixed grid-to-detection-plane separation is used, the optimal grid pitch and hole size are wavelength dependent. To achieve high a signal-to-noise ratio, it is important that the Hartmann grid be opaque in the blocked regions.

Between these two complementary and compatible approaches, Hartmann has greater capacity to measure large aberrations, while shearing offers tunable high sensitivity for small aberrations and a higher measurement point density.

While both approaches are proven and effective, developing wavefront sensors for high-coherent-flux beamlines presents challenges that have forced us to consider alternative implementations. The most significant issue is high power and power density; and the second is small beam width, below 1 mm in some cases.

To our knowledge, all shearing and Hartmann applications on soft x-ray beamlines have used transmission elements made

with patterned thin foils (Hartmann) or absorber-coated membranes (shearing)—Si or Si<sub>3</sub>N<sub>4</sub>—with  $\sim 1\ \mu\text{m}$  thickness. For our applications, we calculate that due to poor thermal conductivity, absorbing approximately  $0.5\ \text{W}$  in  $1\ \text{mm}^2$ , in a  $3\ \text{mm}$  wide membrane, would increase membrane temperatures by hundreds to thousands of degrees [9], melting them. Therefore, an alternative, thermally robust mechanism for wavefront sensor gratings must be developed for the new generation of beamlines.

Gratings used at glancing incidence are a common feature in x-ray monochromators where they serve as a dispersive element, enabling energy selection and filtering. Small angles of incidence spread the beam footprint in the tangential direction (the direction of propagation), reducing the power density. Thick substrates promote heat dissipation and active cooling, where necessary. However, monochromator grating structures, whether they are blazed or lamellar, primarily modify the phase of the beam by encoding spatially varying path lengths. Amplitude modulation for those gratings is a secondary consideration connected to the diffraction efficiency. It can arise from shadowing in the three-dimensional structure.

Phase-shifting properties can be adapted to reflection-mode shearing gratings using a height-relief structure. Gratings would function like transmission phase gratings at normal incidence, but would use an off-axis detector geometry (Fig. 1). The phase change upon reflection from a surface of depth  $h$  is [10]

$$\Delta\phi = \frac{4\pi}{\lambda} h \sin\theta. \quad (1)$$

Wavelength dependence complicates fabrication significantly, forcing a range of etch depths to be used. For wavelengths from  $0.5\ \text{nm}$  to  $5\ \text{nm}$ , with  $1^\circ$  incidence, achieving  $\pi/4$  phase shift (for example) requires depths from  $1.8\ \text{nm}$  to  $18\ \text{nm}$ —challenging to achieve on a single device. However, most importantly, creating *amplitude* modulation with high contrast and opacity for Hartmann testing requires a different grating structure: unwanted light must be redirected or blocked.

Our solution is to deeply etch a binary pattern that includes a series of regularly-spaced horizontal walls as barriers, to intercept and block light (Fig. 2). Light reflected from the top surface of the structure propagates onward, while the transverse walls intercept all other rays, either directly, or after reflection from the lower surface.

The relationship between the largest angle of incidence,  $\theta$ , the tangential distance between walls,  $L$ , and the minimum wall depth,  $a$ , arises from the path of the extreme ray (Fig. 2c): the ray that just clears the wall on the left. To block the incident

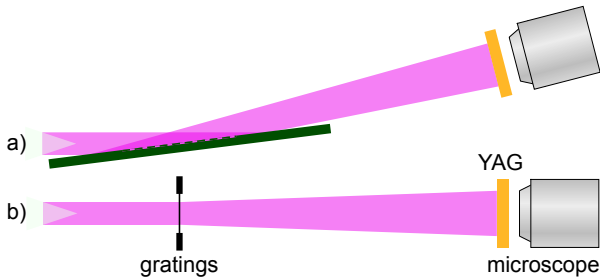


**Fig. 1.** Schematic shearing and Hartmann wavefront sensor geometries with the grating (a) in reflection, and (b) in transmission. In practice, the reflection-grating length will be small relative to the distance from the grating to the detection plane. A microscope and camera system are described in Ref. [4].

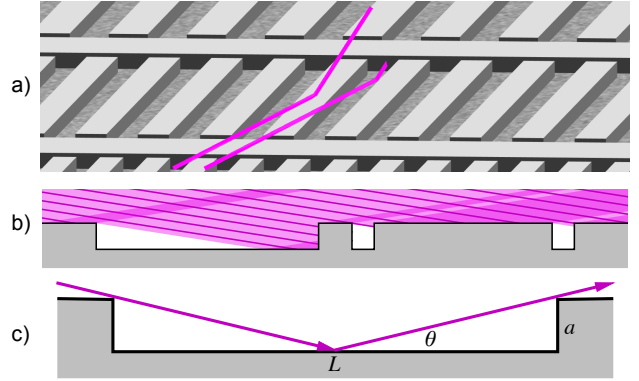


**Fig. 2.** (a) 3D pattern detail showing glancing rays reflected or blocked. (b) Sagittal cross-section of two grating regions illuminated from the upper left. Only light reflected from the top surface propagates onward; walls block all other light. (c) Trajectory of the extreme ray shows geometry for determining the minimum wall height given  $L$  and  $\theta$ .

rays that miss the top surface, we require  $a > \frac{1}{2} L \tan\theta$  (typically,  $a > 10\ \mu\text{m}$ ). A ray-optics approach is justified with pattern sizes ranging from  $10^3$  to  $10^6$  larger than the maximum wavelength. A deeper etch allows the spacing between walls to be increased.

Glancing-incidence effectively foreshortens the pattern in the tangential direction, reducing the feature sizes by a factor  $\sin\theta$ , which is  $1/57.3$  at  $1^\circ$ . Light reflected from the top surface of the walls appears weakly in the recorded images, but having no horizontal features, it does not degrade the measurement of 1D grating patterns. Here, a  $198\ \mu\text{m}$  wide wall diffracts light like a  $3.5\ \mu\text{m}$  slit. For soft x-ray photon energies, a  $5\ \mu\text{m}$  wide wall would be sufficiently opaque: it would diffract like an  $87\ \text{nm}$  slit, and would occupy less than  $0.5\%$  of the pattern area.

One- and two-dimensional gratings can be designed using this approach, with the pattern elongated in the tangential direction to accommodate the glancing angle of incidence. Our prototype will provide 1D wavefront-correction feedback for a bendable, glancing-incidence adaptive x-ray mirror that is capable of tangential shape adjustment. As such, the pattern contains only one-dimensional shearing gratings and Hartmann grids. Note that for 2D patterns, the walls could be incorporated into the useful aspects of the design.

Surface quality is only a significant consideration for the top level where the device functions as an x-ray mirror. This is further discussed below. The quality of the lower surface is of little consequence because light reflected from that region is blocked by the walls. However, since unwanted light scattered from roughness on the lower surface could reach a downstream detector, increasing the wall height could provide greater angular separation and scattered light mitigation.

A photograph of a grating array chip is shown in Fig. 3. Gratings  $3\ \text{mm}$  wide exceed the beam width in our application. In the tangential direction, the beam illuminates a column of ten gratings or grids all at once. Each grating's pitch is optimized for a different central wavelength. A full column of illuminated patterns will be projected onto the detector plane, to appear in the recorded image; the appropriate wavelength-matched grating or grid can then be selected from the array for analysis.

In this grating array, the three left columns contain ten shearing gratings each. The fourth column contains eight Hartmann grids and a test region, described below. The fifth column is a

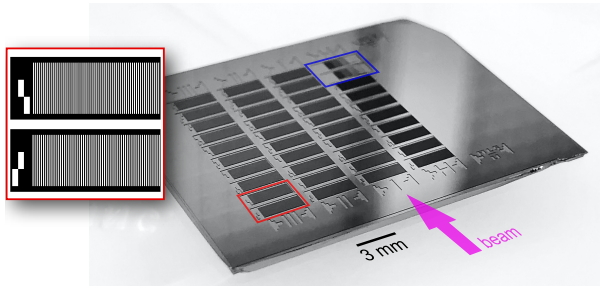


**Fig. 3.** Photograph of etched patterns on a grating chip cleaved from a 6-inch Si wafer. The die has 38 individual  $3 \times 1$  mm gratings and an open mirror area. A pattern detail (red outline) shows two gratings with alignment marks. Etched regions are shown in black. Test gratings designed for reflectometry are outlined in blue and described in Fig. 5.

blank, mirror region. The gratings and grids are designed for a fixed grating-to-detector distance of approximately 300 mm. At glancing incidence, this is a conical diffraction geometry. Shearing grating design for the equivalent transmission geometry is described in Refs. [2], [4], [5]. The shearing gratings have 50% duty cycle (i.e. equal lines and spaces) and pitch values from  $49 \mu\text{m}$  to  $16 \mu\text{m}$  to span the photon energy range 170 eV to 1583 eV (7.29 nm to 0.78 nm wavelength). The Hartmann grids have duty cycle of 22.5% and span the same range.

While they are designed for specific energies, the individual grids and gratings can operate over narrow bands [4]. Our studies show that in this design, Hartmann grids can operate 17.5% below the design energy before adjacent beamlets overlap. Owing to the Talbot condition, the usable range for amplitude-modulating shearing gratings is closer to  $\pm 4\%$ . This issue should be addressed, case-by-case, for alternate designs.

Shearing grating design [3–5] and Hartmann grid design [4, 6] have been described by several groups, including the approach of using an array of gratings in transmission, and utilizing fractional Talbot planes. Using multiple Talbot planes can reduce the number of unique gratings required in an array.

Gratings were fabricated from single-side-polished, prime-grade,  $675 \mu\text{m}$ -thick, silicon wafers. Patterns were transferred using a DUV photolithography stepper, followed by reactive ion etching to strip a thermal oxide hard mask, and a deep reactive-ion etch to achieve depths greater than  $20 \mu\text{m}$  [11].

While light interferometry was used to characterize the surface topography in the clear areas and the etched regions (Fig. 4). Observed rms and peak-to-valley (PV) variations in  $100 \times 50 \mu\text{m}$  regions are shown. The etched regions reach a depth of approximately  $29 \mu\text{m}$  in the wide areas, and  $25.6 \mu\text{m}$  between the grating lines. With the prototype's  $1.067 \text{ mm}$  between horizontal walls ( $L$ ) and  $1^\circ$  angle of incidence ( $\theta$ ), this depth exceeds the minimum requirement ( $\frac{1}{2}L \tan \theta$ ) of  $9.3 \mu\text{m}$  by a factor of 2.75.

Each  $3 \times 1$  mm grating is intended to be interpreted separately during 1D wavefront measurements, thus surface quality requirements apply locally to these small regions. Furthermore, small, tangential slope errors will not distort the 1D fringe patterns. For  $1^\circ$  incidence, achieving an uncalibrated  $\lambda/20$  rms path length error upon reflection (for example) requires a surface quality of  $\sigma = 1.43 \lambda$ . Thus, 1 nm surface roughness would meet this requirement for wavelengths down to 0.7 nm (1771 eV).

Two-dimensional wavefront measurements would require high surface quality to be achieved—or the device to be

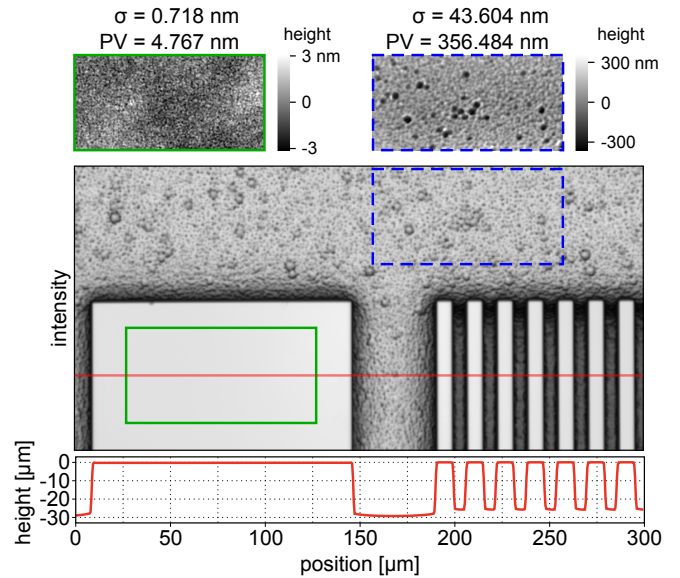


**Fig. 4.** Surface characterization with white-light interferometry. The intensity image (central portion) shows a pattern of etched regions surrounding protected top-surface areas. The grating lines have  $16 \mu\text{m}$  pitch. Individually scaled surface height map details ( $100 \times 50 \mu\text{m}$ ) are extracted from the clear area (green outline) and from the etched region (blue dash). A cross-sectional height plot is calculated from a vertical average over  $50 \mu\text{m}$ , centered about the red line. The contour is plotted isometrically, to show the depth relative to the lateral size.

calibrated—across the full beam footprint.

The device was measured with soft x-ray light at the Advanced Light Source. Glancing-incidence reflectance reveals the efficacy of the binary amplitude structure in blocking the unwanted light. The monochromatic beam ( $E/\Delta E = 1000$ ) has a spot size of  $120 \times 40 \mu\text{m}$  at focus. Using a 2 mm photodiode to detect the reflected power, the beam was vertically centered on the horizontal wall between two identical grating regions and scanned across the pattern (Fig. 5). The size of the tangential beam footprint changed as the angle of incidence was varied from  $1^\circ$  to  $4^\circ$ .

The five regions of the test-grating pattern have constant  $32 \mu\text{m}$  pitch and duty cycle values varying from 0% (dark) to 100% (bright). Measurements were made at photon energies 500 eV (2.48 nm) and 750 eV (1.65 nm). While the prototype was designed to operate at  $1^\circ$ , we measured with incidence angles of  $\{1^\circ, 1.5^\circ, 2^\circ, 2.5^\circ, 3^\circ, \text{ and } 4^\circ\}$  to test the useful operating range.

The scan data were analyzed in the following way. Reflection from the top of the wall produces a constant light-background signal that is measured in the 0% duty-cycle region; that signal defines the *zero* point and is subtracted from the others. The signal from the center of the 100% duty-cycle region defines the *maximum* value, used to normalize the measurements. The scaled signal recorded at the center of each of the three gratings then reveals the reflected fraction, which should follow the duty cycle if the device is effectively blocking unwanted light (Fig. 6).

For the two photon energies, 500 eV and 750 eV, respectively, the attenuation lengths in Si are  $0.43 \mu\text{m}$  and  $1.22 \mu\text{m}$  [12], and in the unpatterned area, the measured reflectivities at  $1^\circ$  are  $0.841 \pm 0.002$  and  $0.845 \pm 0.002$ .

A coherent wave model (Fig. 7) demonstrates shearing in-

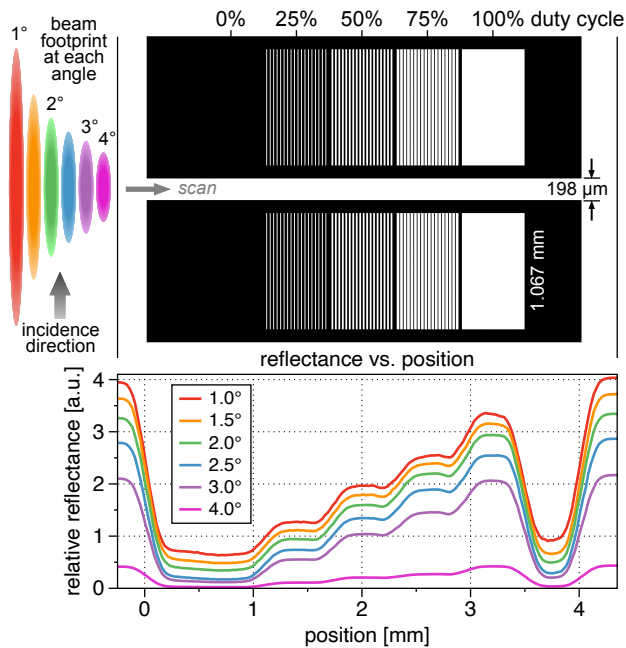


**Fig. 5.** Grating test region with etched areas in black. Gratings have constant pitch and five duty cycle values. Approximate footprints of the focused soft x-ray beams are shown for six angles of incidence. Reflected power is measured as the beam is scanned horizontally across the pattern. For 500 eV photon energy, relative reflectance for six incidence angles is shown, aligned with the gratings, above; the critical angle is  $3.48^\circ$  [12].

terferometry of a 1.267 nm wavelength Gaussian beam at  $1^\circ$  incidence. The transverse intensity FWHM is  $833 \mu\text{m}$ . Of the ten different gratings, the Talbot condition is met in the 5<sup>th</sup> row from the bottom, with  $19.5 \mu\text{m}$  pitch, 300 mm downstream.

This work demonstrates glancing incidence reflection x-ray gratings with binary amplitude modulation, made with deep etching and pattern features that block unwanted light. These optical elements are well-suited for shearing interferometry gratings and Hartmann wavefront sensor grids, and possibly structured illumination, and arbitrary holographic or diffraction-pattern applications where the incident beam's power density is too high for thin transmission elements. Arrays of features enable the devices to be used across a broad energy range.

**FUNDING.** This work was supported by the Director, Office of Science, Office of Basic Energy Sciences, of the U.S. Department of Energy under Contract No. DE-AC02-05CH11231.

**ACKNOWLEDGMENT.** The authors appreciate the support of Howard Padmore and Elaine DiMasi of LBNL. Daniel Contreras and Min He of AMFitzgerald fabricated the gratings. Ian Lacey of LBNL assisted with surface metrology.

## REFERENCES

1. P. P. Naulleau, K. A. Goldberg, and J. Bokor, *J Vac Sci & Technol B* **18**, 2939 (2000).
2. S. Matsuyama, H. Yokoyama, R. Fukui, Y. Kohmura, K. Tamasaku, M. Yabashi, W. Yashiro, A. Momose, T. Ishikawa, and K. Yamauchi, *Opt. Express* **20**, 24977 (2012).

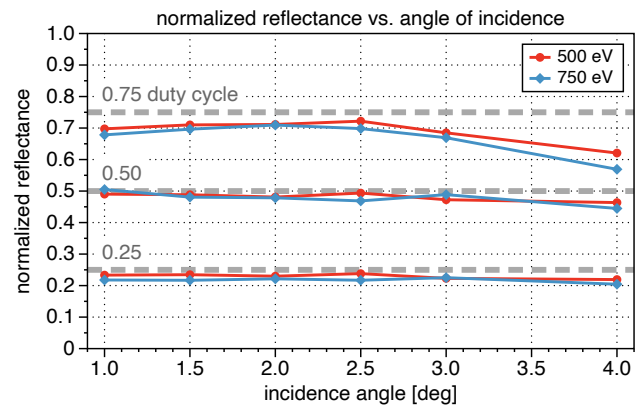


**Fig. 6.** Reflected light fraction from the 25%, 50%, and 75% duty-cycle gratings, extracted from the scans (Fig. 5) and plotted versus angle of incidence. The design angle is  $1^\circ$ . Maximum uncertainty is 0.7% for 750 eV and 1.0% for 500 eV.

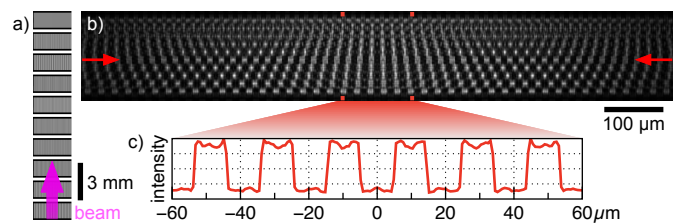


**Fig. 7.** Coherent model of a recorded shearing interferogram at 1.267 nm wavelength, from the array's 3<sup>rd</sup> column. (a) The 10-row grating pattern: etched regions are shown in black. (b) Central 1 mm interferogram detail. Red arrows mark the row where the intensity cross-section (c) is extracted. The  $1^\circ$  incidence angle accounts for a 57.3:1 foreshortening.

3. D. J. Merthe, V. V. Yashchuk, K. A. Goldberg, M. Kunz, N. Tamura, W. R. McKinney, N. A. Artemiev, R. S. Celestre, G. Y. Morrison, E. H. Anderson, B. V. Smith, E. E. Domning, S. B. Rekawa, and H. A. Padmore, *Opt. Eng.* **52**, 1 (2013).
4. A. Wojdyla, D. Bryant, W. Chao, L. Assoufid, D. Cocco, M. Idir, and K. A. Goldberg, *Proc. SPIE* **10760**, 1076003 (2018).
5. M. Seaberg, R. Cojocaru, S. Berujon, E. Ziegler, A. Jaggi, J. Krem-pasky, F. Seiboth, A. Aquila, Y. Liu, A. Sakdinawat, H. J. Lee, U. Flechsig, L. Patthey, F. Koch, G. Seniutinas, C. David, D. Zhu, L. Mikeš, M. Makita, T. Koyama, A. P. Mancuso, H. N. Chapman, and P. Vagovič, *J. Synchrotron Radiat.* **26**, 1115 (2019).
6. P. Mercère, P. Zeitoun, M. Idir, S. Le Pape, D. Douillet, X. Levecq, G. Dovillaire, S. Bucourt, K. A. Goldberg, P. P. Naulleau, and S. Rekawa, *Opt. Lett.* **28**, 1534 (2003).
7. M. Idir, P. Mercere, M. H. Modi, G. Dovillaire, X. Levecq, S. Bucourt, L. Escolano, and P. Sauvageot, *Nucl. Instruments Methods Phys. Res. A* **616**, 162 (2010).
8. S. Marathe, X. Shi, M. J. Wojcik, N. G. Kujala, R. Divan, D. C. Mancini, A. T. Macrander, and L. Assoufid, *Opt. Express* **22**, 14041 (2014).
9. R. T. Balmer, *Modern Engineering Thermodynamics* (Academic Press, Boston, 2011).
10. E. L. Church and P. Z. Takacs, *Opt. Eng.* **34**, 353 (1995).
11. M. J. Madou, *Fundamentals of Microfabrication and Nanotechnology*, vol. II (CRC Press, Taylor & Francis Group, 2012), 3rd ed.
12. [http://henke.lbl.gov/optical\\_constants/](http://henke.lbl.gov/optical_constants/). CXRO, index of refraction data.

## FULL REFERENCES

1. P. P. Naulleau, K. A. Goldberg, and J. Bokor, "Extreme ultraviolet carrier-frequency shearing interferometry of a lithographic four-mirror optical system," *J Vac Sci & Technol B* **18**, 2939–6 (2000).
2. S. Matsuyama, H. Yokoyama, R. Fukui, Y. Kohmura, K. Tamasaku, M. Yabashi, W. Yashiro, A. Momose, T. Ishikawa, and K. Yamauchi, "Wavefront measurement for a hard-X-ray nanobeam using single-grating interferometry," *Opt. Express* **20**, 24977–24986 (2012).
3. D. J. Merthe, V. V. Yashchuk, K. A. Goldberg, M. Kunz, N. Tamura, W. R. McKinney, N. A. Artemiev, R. S. Celestre, G. Y. Morrison, E. H. Anderson, B. V. Smith, E. E. Domning, S. B. Rekawa, and H. A. Padmore, "Methodology for optimal in situ alignment and setting of bendable optics for nearly diffraction-limited focusing of soft x-rays," *Opt. Eng.* **52**, 1–14 (2013).
4. A. Wojdyla, D. Bryant, W. Chao, L. Assoufid, D. Cocco, M. Idir, and K. A. Goldberg, "Design and demonstration of tunable soft x-ray lateral shearing and Hartmann wavefront sensors," *Proc. SPIE* **10760**, 1076003 (2018).
5. M. Seaberg, R. Cojocar, S. Berujon, E. Ziegler, A. Jaggi, J. Krempasky, F. Seiboth, A. Aquila, Y. Liu, A. Sakdinawat, H. J. Lee, U. Flechsig, L. Patthey, F. Koch, G. Seniutinas, C. David, D. Zhu, L. Mikeš, M. Makita, T. Koyama, A. P. Mancuso, H. N. Chapman, and P. Vagovič, "Wavefront sensing at X-ray free-electron lasers," *J. Synchrotron Radiat.* **26**, 1115–1126 (2019).
6. P. Mercère, P. Zeitoun, M. Idir, S. Le Pape, D. Douillet, X. Levecq, G. Dovillaire, S. Bucourt, K. A. Goldberg, P. P. Naulleau, and S. Rekawa, "Hartmann wave-front measurement at 13.4 nm with  $\lambda_{EUV}/120$  accuracy," *Opt. Lett.* **28**, 1534 (2003).
7. M. Idir, P. Mercere, M. H. Modi, G. Dovillaire, X. Levecq, S. Bucourt, L. Escolano, and P. Sauvageot, "X-ray active mirror coupled with a Hartmann wavefront sensor," *Nucl. Instruments Methods Phys. Res. A* **616**, 162–171 (2010).
8. S. Marathe, X. Shi, M. J. Wojcik, N. G. Kujala, R. Divan, D. C. Mancini, A. T. Macrander, and L. Assoufid, "Probing transverse coherence of x-ray beam with 2-D phase grating interferometer," *Opt. Express* **22**, 14041–13 (2014).
9. R. T. Balmer, *Modern Engineering Thermodynamics* (Academic Press, Boston, 2011).
10. E. L. Church and P. Z. Takacs, "Specification of glancing- and normal-incidence x-ray mirrors," *Opt. Eng.* **34**, 353–360 (1995).
11. M. J. Madou, *Fundamentals of Microfabrication and Nanotechnology*, vol. II (CRC Press, Taylor & Francis Group, 2012), 3rd ed.
12. [http://henke.lbl.gov/optical\\_constants/](http://henke.lbl.gov/optical_constants/). CXRO, index of refraction data.